

# Nanoscale

Accepted Manuscript



This is an *Accepted Manuscript*, which has been through the Royal Society of Chemistry peer review process and has been accepted for publication.

*Accepted Manuscripts* are published online shortly after acceptance, before technical editing, formatting and proof reading. Using this free service, authors can make their results available to the community, in citable form, before we publish the edited article. We will replace this *Accepted Manuscript* with the edited and formatted *Advance Article* as soon as it is available.

You can find more information about *Accepted Manuscripts* in the [Information for Authors](#).

Please note that technical editing may introduce minor changes to the text and/or graphics, which may alter content. The journal's standard [Terms & Conditions](#) and the [Ethical guidelines](#) still apply. In no event shall the Royal Society of Chemistry be held responsible for any errors or omissions in this *Accepted Manuscript* or any consequences arising from the use of any information it contains.

## ARTICLE

# Chemically doped three-dimensional porous graphene monoliths for high-performance flexible field emitters

Cite this: DOI: 10.1039/x0xx00000x

Received 00th January 2013,  
Accepted 00th January 2013

DOI: 10.1039/x0xx00000x

www.rsc.org/

Ho Young Kim,<sup>ab</sup> Sooyeon Jeong,<sup>c</sup> Seung Yol Jeong,<sup>c</sup> Kang-Jun Baeg,<sup>a</sup> Joong Tark Han,<sup>a</sup> Mun Seok Jeong,<sup>\*b</sup> Geon-Woong Lee<sup>\*a</sup> and Hee Jin Jeong,<sup>\*ac</sup>

Despite the recent progress in the fabrication of field emitters based on graphene nanosheets, their morphological and electrical properties, which affect their degree of field enhancement as well as the electron tunnelling barrier height, should be controlled to allow for better field-emission properties. Here we report a method that allows the synthesis of graphene-based emitters with a high field-enhancement factor and a low work function. The method involves forming monolithic three-dimensional (3D) graphene structures by the freeze-drying of a highly concentrated graphene paste and subsequent work-function engineering by chemical doping. Graphene structures with vertically aligned edges were successfully fabricated by the freeze-drying process. Further, their number density could be controlled by varying the composition of the graphene paste. Al- and Au-doped 3D graphene emitters were fabricated by introducing the corresponding dopant solutions into the graphene sheets. The resulting field-emission characteristics of the resulting emitters are discussed. The synthesized 3D graphene emitters were highly flexible, maintaining their field-emission properties even when bent at large angles. This is attributed to the high crystallinity and emitter density and good chemical stability of the 3D graphene emitters, as well as to the strong interactions between the 3D graphene emitters and the substrate.

## Introduction

Because graphene has a two-dimensional (2D) structure consisting of single-atom-thick layers and a high aspect ratio (ratio of the lateral size to the thickness) as well as high flexibility without significant degradation in electrical properties, it exhibits excellent field-emission characteristics. This makes it a good material for use as the emitter in field-emission devices (FEDs).<sup>1,2</sup> Since electrons are emitted primarily from the tops of the graphene edges, where the electric field is very strong during field emission,<sup>2,3</sup> a prerequisite for the graphene structures used in flexible FEDs is that the graphene be vertically aligned or at least protrude from the polymeric substrate. However, this is not a trivial requirement, because 2D graphene sheets tend to form parallel to the substrate during deposition. Therefore, a number of methods for fabricating vertically aligned graphene structures on substrates, such the electrophoresis of a charged graphene solution, the spin-casting of graphene/polymer composites, direct growth, self-assembly, filtering, and thermal welding, are being explored to develop high-performance graphene emitters.<sup>1,2,4–11</sup>

In addition to this structural modification of graphene to maximize the field emissions from its edges, control over the work function of the intrinsic graphene is also important for controlling the field-emission characteristics, because the physical properties of the emitter material have a significant effect on the tunnelling barrier at the interface between the material surface and vacuum. Chemical doping can be a useful approach for modulating the work function of graphene because the intrinsic Fermi level of graphene can be readily shifted, owing to charge transfer between the dopant and graphene.<sup>12–17</sup> However, only the effects of varying the work function on the electrical properties, conductivity, and charge density have been studied, and its influence on the field-emission properties has not been investigated adequately.

Further, electron emitters that exhibit long-duration and stable emissions are a prerequisite for high-quality FEDs suitable for practical use, because nanocarbon-based electron emitters are easily damaged by the bombardment of ions of the residual gas species, which are degassed from the getters, inner walls, and phosphors.<sup>18</sup> This results in degradation of the field-emission properties such as the brightness, uniformity, and lifetime. To prevent this, thin films of semiconducting metal

oxides with low gas permeabilities can be used as protection layers for graphene-based field emitters.

This study had three main aims. The first was to enhance the field emissions from graphene-based electron emitters by using three-dimensional (3D) monolithic graphene structures with random micropores formed by the freeze-drying of highly concentrated water-based reduced graphene oxide (rGO)/polymer pastes. The aligned porous structures with numerous sharp graphene edge sites were produced by the phase separation of water and the polymer owing to the Mullins-Sekerka instability and the growth of ice cells.<sup>19,20</sup> The second was to modulate the work functions of the 3D rGO electron emitters via chemical doping. The effects of this work-function engineering on the field-emission characteristics were investigated. The third was to enhance the stability of the emissions of the 3D rGO electron emitters. This was accomplished by forming a protective zinc oxide (ZnO) layer. By achieving these goals, we were able to synthesize flexible high-performance nanocarbon-based field emitters.

## Results and discussion

Highly concentrated water-based rGO pastes (see Fig. 1a) could be prepared, owing to the monovalent cation- $\pi$  interactions of the rGO sheets, as has been reported previously.<sup>21</sup> The rGO nanosheets were approximately  $10 \mu\text{m}^2$  in size and  $\sim 1 \text{ nm}$  in thickness, which corresponded to a single layer of graphene, as shown in the inset. Owing to the cation- $\pi$  interaction between the monopoles ( $\text{Na}^+$  and  $\text{K}^+$  ions) and quadrupoles (aromatic  $\pi$  system), the rGO films exhibited an electrical conductivity of  $\sim 100,000 \text{ S/m}$ . This was because of the effect of the doping of monovalent ions in the rGO sheets as well as the high dispersion stability of the ions in the solution. A 3D porous rGO structure<sup>22–24</sup> was prepared by the simple bar coating of the

rGO paste and its subsequent freeze-drying, as illustrated in Fig. 1b. During the bar-coating process, the thickness of the layer of rGO paste was controlled by the height of the template. To increase the viscosity and printability of the rGO paste, 1 wt% sodium carboxymethylcellulose (SCMC) was added to it. SCMC, a water-soluble polymer, is an ionic polysaccharide derived from cellulose and contains numerous hydroxyl and carboxylic acid moieties, which provide strong physical bonding to the polymer matrix because of the substituted sodium ions. Moreover, SCMC is employed as a flow enhancer, stabilizer, and as a binding, suspending and thickening agent.<sup>25,26</sup> Subsequently, freezing was performed by immersing the bar-coated layer of rGO paste in a liquid nitrogen bath. During the freezing process, ice crystals grew and the rGO/SCMC mixture was removed from the frozen water until the sample was completely frozen. Because the rGO/SCMC mixture had an extremely low solubility in the ice crystals, a gradient in the concentration of the rGO/SCMC mixture was created. The concentration of the rGO/SCMC mixture ahead of the ice front increased.<sup>27</sup> This reduced the melting point of the solution, resulting in the formation of a constitutional supercooling zone. This broke the planar interface, and the ice cell could grow vertically.<sup>28</sup> This phenomenon is called the Mullins-Sekerka instability, according to which the primary ice-template structure is dependent on the interfacial concentration gradient of the destabilizing solute and the surface energy opposing cell formation. The extremely low-temperature freezing using liquid nitrogen at  $-196 \text{ }^\circ\text{C}$ , which is well below the glass transition temperature of water ( $-137 \text{ }^\circ\text{C}$ ), results in the rapid formation of ice nuclei and hence the growth of relatively small ice crystals. After the sublimation of the vertically grown ice crystals by vacuum drying, monolithic 3D rGO structures with cylindrical pores (Fig. 1d) could be obtained. Figure 1c shows foam-like macrostructures consisting

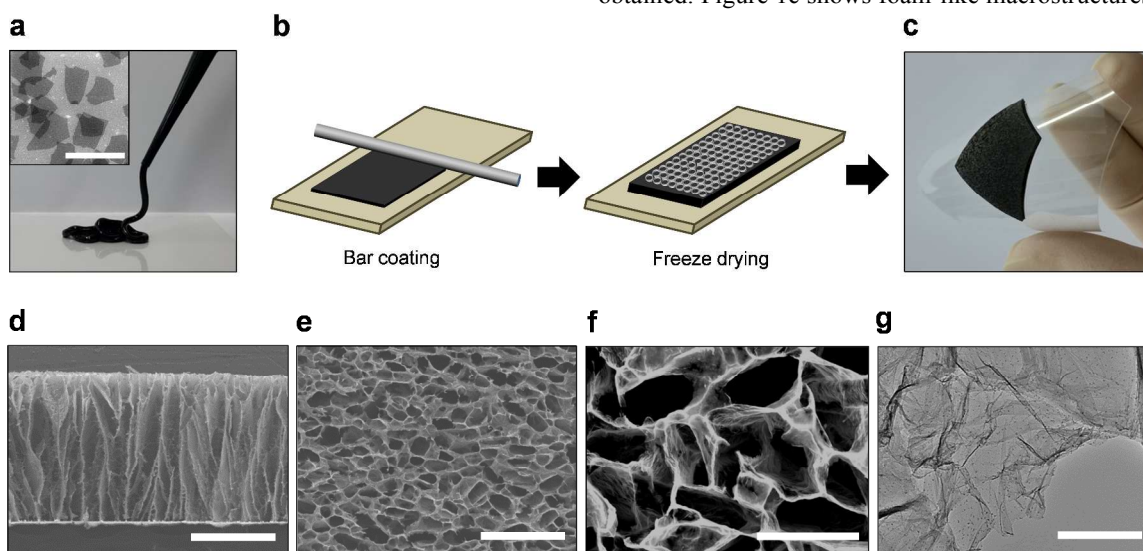


**Fig. 1.** (a) Photograph of a highly concentrated water-based rGO paste. Inset shows SEM image of rGO sheets in the paste. The scale bar is  $5 \mu\text{m}$ . (b) Schematic of fabrication of monolithic 3D rGO structure by the bar coating of a rGO paste and subsequent freeze-drying. (c) Photograph of a 3D rGO structure fabricated on a flexible polymer substrate. (d) Cross-sectional SEM images of a 3D rGO structure. The scale bar is  $300 \mu\text{m}$ . (e) and (f) Top-view SEM images with low and high magnifications, respectively. The scale bars are  $300 \mu\text{m}$  and  $100 \mu\text{m}$ , respectively. (g) TEM image of stacked rGO nanosheets. The scale bar is  $400 \text{ nm}$ .

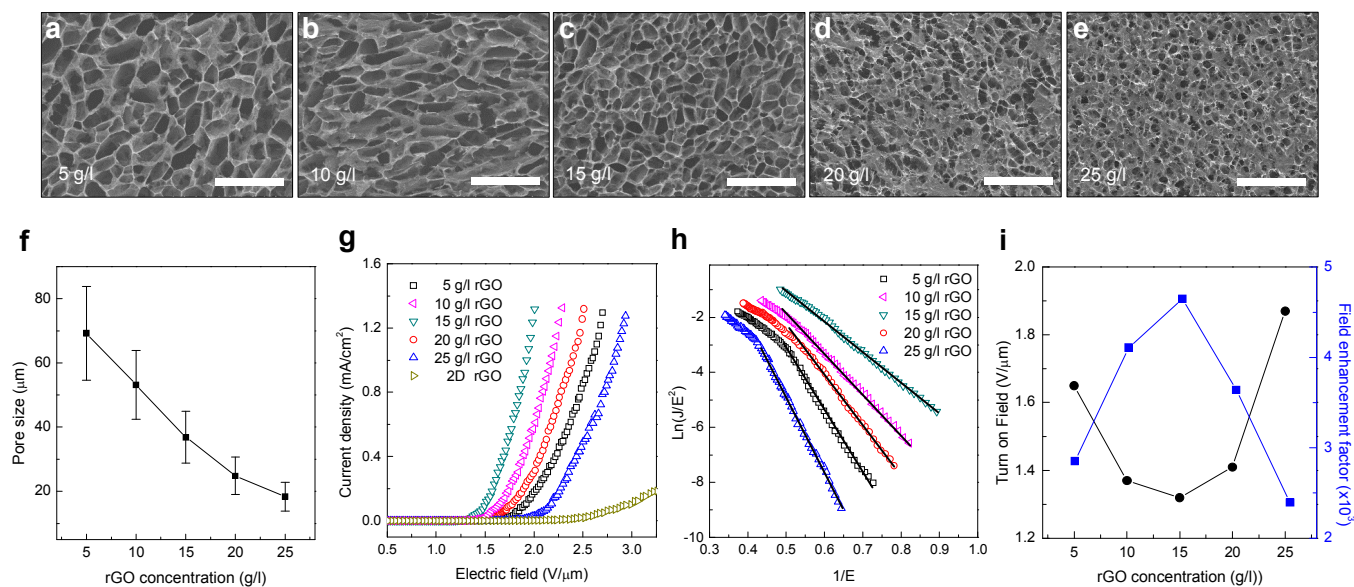


**Fig. 2.** (a)–(e) SEM images of the 3D rGO structures fabricated using different rGO concentrations. The scale bars indicate 300 μm. (f) Pore size distributions of the 3D rGO structures as a function of the rGO concentration. (g)  $J$ – $E$  characteristics of the 3D rGO emitters fabricated using various rGO concentrations, and (h) their F–N plots. (i) The turn-on fields and field-enhancement factors as functions of the rGO concentration.

of uniformly distributed rGO sheets strongly attached on the flexible substrate. The 3D rGO structure was mechanically robust, flexible, and easy to handle. Although the randomly distributed pores on the top surface of the 3D rGO structure were several tens of micrometres in size (Fig. 1e), the pore walls had numerous sharp edges, which were a few hundred nanometres in size (Fig. 1f). The size, shape, and homogeneity of these pores could be adjusted by choosing different freezing temperatures, solution concentrations, and solvents. The protruding nanometre-sized rGO tips readily emitted electrons under a strong electric, owing to high field enhancement. These sharp edges were mainly composed of stacked structures consisting of the rGO nanosheets, as shown in Fig. 1g.

Figures 2a–e show the surface morphologies of the 3D rGO structures fabricated by the freeze-drying method for different rGO concentrations. The 3D rGO structure corresponding to an rGO concentration of 5 g/L had irregular-shaped pores with an average size of 69.2 μm (Fig. 2a). The pores of the 3D rGO structures gradually decreased in size and became spherical as the concentration of rGO was increased. This was because it became increasingly difficult for ice crystals to form in the presence of impurities (in this case, the rGO/SCMC mixture); this was in keeping with previous results.<sup>29</sup> Finally, the size of the pores decreased to 18.4 μm at an rGO concentration of 25 g/L (Fig. 2e). The average pore size of the synthesized 3D rGO structures is shown as a function of the rGO concentration in Fig. 2f.

The electron field emissions of the 3D rGO emitters were investigated using a diode-type device, which was placed within a vacuum chamber and subjected to a dc bias. Polyethylene terephthalate (PET, 200 μm in thickness) and ITO-coated glass substrates were used as the spacer and anode, respectively. To remove the emission noise and instabilities,

electrical aging involving several steps ( $I$ – $V$  sweeping and high-voltage annealing) was performed until the emission currents showed negligible fluctuations. The current density–electric field ( $J$ – $E$ ) characteristics of the 3D rGO emitters are shown in Fig. 2g. The 3D rGO emitter prepared using an rGO paste with a concentration of 15 g/L (pore size of 36.9 μm) displayed the lowest turn-on field ( $E_{\text{to}}$ : 1.32 V/μm at 10 μA/cm²) and threshold field ( $E_{\text{thr}}$ : 1.92 V/μm at 1 mA/cm²). Further, these values were much lower than those previously reported for graphene and graphite sheet emitters.<sup>1,2,30,31</sup> These results are probably attributable to the high density of the sharp-tipped 3D rGO structures as well as the moderate size of their pores. The edges of the graphene sheets provide the principal electron-emission sites under field-emission conditions.<sup>1–3</sup> The turn-on and threshold fields were found to be much higher for flat-structured 2D rGO films than for the sharp-tipped 3D rGO structures. It is known that electron emission can be enhanced by increasing the aspect ratio of the emitter; however, it is reduced by the field-screening effects arising from the field penetration of the emitters.<sup>32–34</sup> It is, therefore, necessary to optimize the density of the edge sites of the graphene emitter to achieve maximum electron emission. Field emission is generally analyzed using the Fowler–Nordheim (F–N) theory, which describes the tunnelling of electrons through a potential barrier formed at the interface between a solid surface and a vacuum.<sup>35</sup> The F–N theory states that the geometrical field-enhancement factor of an emitter is inversely proportional to the slope of the F–N plot ( $\beta = -B\Phi^{1.5}S^{-1}$ , where  $B$  is a constant,  $\Phi$  is the work function, and  $S$  is the slope). Figure 2h shows the F–N plots of the fabricated 3D rGO emitters, which had different pore sizes. Because we used homogeneous rGO sheets to prepare the 3D rGO structures for the field emitters, the work functions of all the 3D rGO emitters were assumed to be similar.

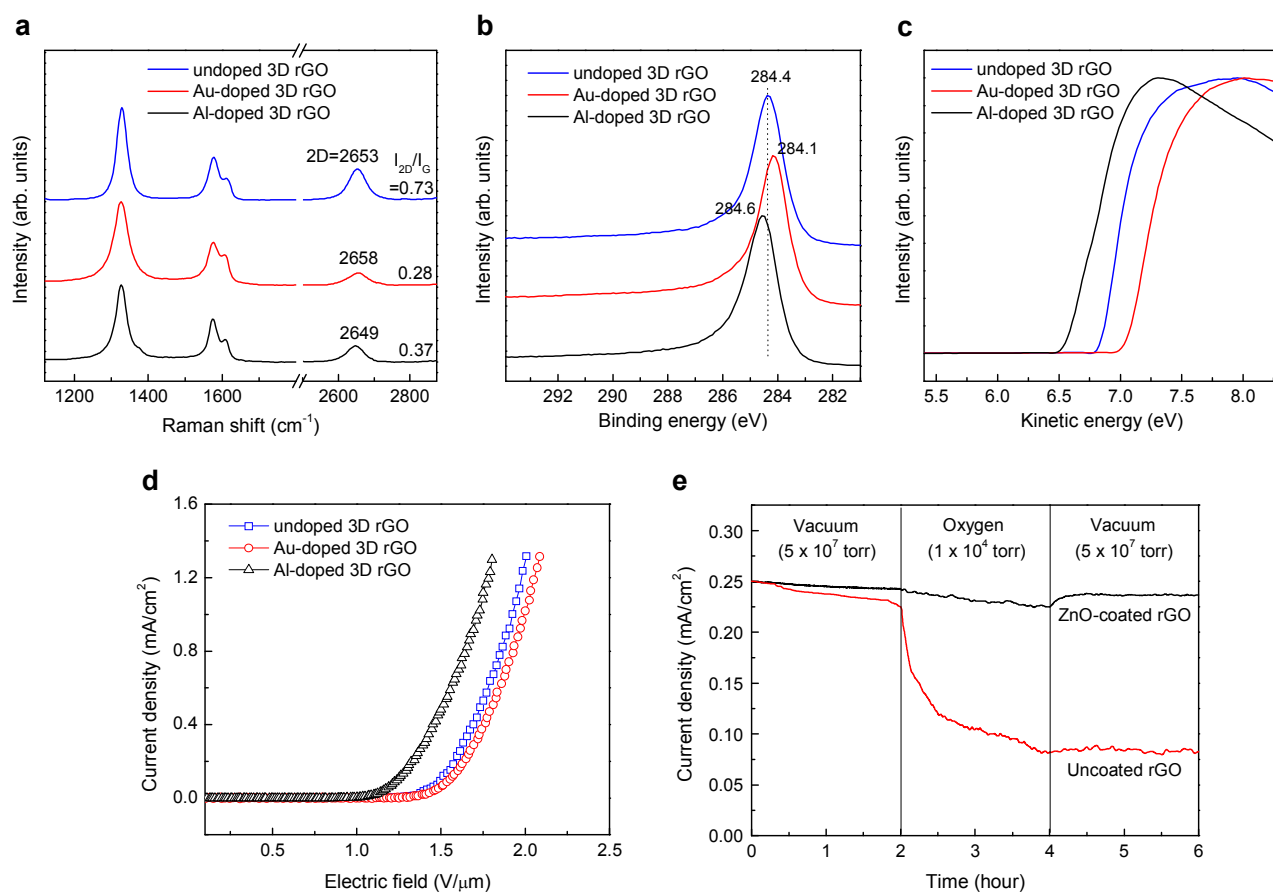


**Fig. 3.** (a) Raman spectra, (b) XPS C1s binding energies, and (c) UPS spectra around the secondary-electron threshold region for the undoped, Au-doped, and Al-doped 3D rGO emitters, and (d) their  $J$ - $E$  characteristics. (e) Current stability of the uncoated and ZnO-coated 3D rGO emitters in vacuum and after exposure to  $O_2$ .

Thus, the field-enhancement factor of the 3D rGO emitter prepared using the 15 g/L rGO paste was the largest. A linear extrapolation of the field-enhancement factors, shown in Fig. 2i, indicated that the maximum field-enhancement factor was 4648. The field enhancement factor was calculated from the F-N equation with the work function (4.53 eV, extracted from the UPS data of Fig. 3c) of the 3D rGO emitters and the constant F-N slope in the low current region. This value was much higher than those of graphene and thin graphite sheets reported previously.<sup>1,2,30,31</sup> This high field enhancement factor allows for sufficient tunnelling of electrons, resulting in high field emission characteristics.

As indicated by the F-N equation, the work function affects the field-emission characteristics. Small work functions result in low barrier heights such that electron tunnelling is enhanced for an applied electric field, which leads to good field-emission characteristics. In order to modulate the work function of the 3D rGO emitters, chemical doping was performed using  $AuCl_3$  as a p-type dopant and  $AlCl_3$  as an n-type dopant. Figure 3a shows the Raman spectra of the doped and undoped 3D rGO samples. The 2D peaks (which represent two-phonon inelastic scattering) at approximately  $2650\text{ cm}^{-1}$ , which were symmetric and did not contain any shoulders, were indicative of single-layered graphene. The intensity ratio of the 2D to G ( $I_{2D}/I_G$ )

bands for the undoped 3D rGO emitter was 0.73; this decreased to 0.28 after Au doping and to 0.37 after Al doping. These values were in accordance with the previous results, which suggested that the intensity of the 2D peak of doped graphene is significantly lower than that of the peak of undoped graphene, irrespective of the dopant used.<sup>36</sup> Moreover, the position of the 2D peak of doped 3D rGO samples was shifted with respect to the peaks of the undoped 3D rGO samples; this could be explained by electron-phonon coupling. Phonon hardening by charge transfer from graphene to  $Au^{3+}$  results in an upshift in the Raman 2D peak, whereas phonon softening by charge transfer from  $Al^0$  to graphene results in a downshift of the 2D peak.<sup>12,37</sup>

The effects of doping on the electronic structure of the 3D rGO samples were also investigated using X-ray photoemission spectroscopy (XPS) analysis, as shown in Figs. 3b and S1. The carbon C1s peak at 284.4 eV for  $sp^2$  carbon in the case of undoped 3D rGO was shifted by 0.3 eV to a lower binding-energy level upon Au doping and by 0.2 eV to a higher binding-energy level upon Al doping, without there being a significant change in the relative atomic percentages of the oxygen-related functional groups. This change in the position of the C1s peak was related to a shift in the Fermi level of the 3D rGO originating from charge transfer from the rGO to the

dopant molecule (and vice versa).<sup>38–40</sup> As a consequence, the work function of the 3D rGO was modulated, as can be seen from the ultraviolet photoelectron spectroscopy (UPS) results in Fig. 3c. The work function,  $\Phi$ , can be determined from the secondary electron threshold energy as follows:  $\Phi = h\nu - E_F + E_{\text{cutoff}}$ , where  $h\nu$ ,  $E_F$ , and  $E_{\text{cutoff}}$  are the photon energy of the excitation light (21.2 eV), the Fermi level edge (23.5 eV in this study), and the inelastic high-binding-energy cutoff, respectively.  $E_{\text{cutoff}}$  was determined by linearly extrapolating the high-binding-energy cutoff region of the UPS spectra. The  $E_{\text{cutoff}}$  value of undoped 3D rGO was determined to be approximately 6.83 eV, which corresponded to a work function of 4.53 eV and was similar to that reported previously.<sup>15,41,42</sup> The work function of 3D rGO increased to 4.76 eV upon Au doping and decreased to 4.25 eV upon Al doping. The measured shift ( $\Delta\Phi = 0.51$  eV) was owing to a change in the Fermi level of 3D rGO because of the charge transfer that occurs upon doping, as shown in Figs. 3a and 3b.

The  $J$ - $E$  characteristics of the doped and undoped 3D rGO emitters are shown in Fig. 3d. The tip morphology and the size of pores of the undoped 3D rGO emitters are similar to that of undoped one, as shown in Fig. S2. The Al-doped rGO emitters exhibited a turn-on field ( $E_{\text{to}}$ : 1.07 V/ $\mu\text{m}$ ) and a threshold field ( $E_{\text{thr}}$ : 1.70 V/ $\mu\text{m}$ ) that were lower than those of the undoped rGO emitters ( $E_{\text{to}}$ : 1.32 V/ $\mu\text{m}$ ;  $E_{\text{thr}}$ : 1.92 V/ $\mu\text{m}$ ). As mentioned previously, the work function and field-enhancement factor of the emitter affect the potential barrier formed at the interface between the metal surface and vacuum. Therefore, to ensure a high emission current, the emitter should have a low work function and sharp tips so that the field-enhancement factor is high. This explains why the Al-doped 3D rGO emitter exhibited lower turn-on and threshold fields than did the undoped 3D rGO emitter. It is interesting to note that the turn-on field ( $E_{\text{to}}$ : 1.37 V/ $\mu\text{m}$ ) and threshold field ( $E_{\text{thr}}$ : 1.96 V/ $\mu\text{m}$ ) of the Au-doped 3D rGO emitter were similar to those of the undoped RGO emitter. Since the work function of the Au-doped 3D rGO emitter was higher than that of the undoped 3D rGO emitter, as shown in Fig. 3c, the field-emission characteristics of the Au-doped 3D rGO emitter were poorer than those of the undoped 3D rGO emitter. This may be attributed the conductivity of the Au-doped 3D rGO being higher than of the undoped 3D rGO.<sup>43–45</sup>

The emission stabilities of the 3D rGO emitters in vacuum and in an  $\text{O}_2$  environment are shown in Fig. 3e. When the emitters were initially placed in vacuum, over the first 2 h, the current density decreased slightly (by 10%). However, it decreases significantly (by 70%) after exposure to  $\text{O}_2$  and failed to recover to its initial value even after the complete removal of  $\text{O}_2$ . This could be ascribed to the bombardment of the ions of the oxidative gas species under the high electric field, as is the case with SWNT emitters.<sup>46,47</sup> This instability of the emission current can be prevented by forming a coating of a ZnO sol as a protective layer. ZnO is an n-type semiconductor with a wide band gap, is conductive, and has a low resistivity (of order of  $10^{-2}$  to  $10^{-3}$   $\Omega$  cm).<sup>48–50</sup> The formation of a ZnO protective layer was facilitated by hydrogen bonding between the amine

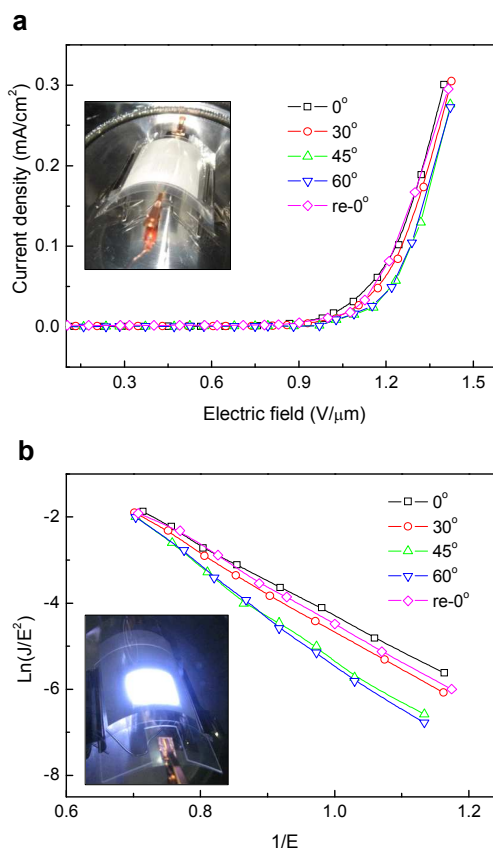


**Fig. 4.** (a)  $J$ - $E$  characteristics and (b) the corresponding  $F$ - $N$  plots of the Al-doped 3D rGO emitters with respect to the bending angle. Insets show images of Al-doped 3D rGO emitter-based flexible FEDs bent at an angle of 30°; the images were obtained before and after an electric field of 1.38 V/ $\mu\text{m}$  was applied, respectively.

groups of the ZnO sol and the carboxyl groups of the rGO nanosheets. Indeed, the stability of the emission current improved drastically after the formation of a ZnO protective layer on the 3D rGO emitters. Unlike the emission currents of the uncoated 3D rGO emitters, those of the ZnO-coated 3D rGO emitters were slightly lower during  $\text{O}_2$  exposure but recovered fully to their initial values after the removal of  $\text{O}_2$ . This might be due to the protection of the emission sites of the 3D rGO emitters from reactive-ion bombardment, because ZnO is known to be robust and inert.

Figure 4 shows the field-emission characteristics of the flexible 3D rGO emitters. In this case, the emitters were fabricated by the freeze-drying of the Al-doped rGO paste coated on PET substrates. A 500-mm-thick PET film was used as the spacer and a white phosphor-coated SWNT layer on a PET substrate was used as the anode, as shown in the inset of Fig. 4a.<sup>51</sup> The dc-pulse mode (duty cycle of 20%) was used to minimize structural damage to the emitters and to prevent changes to the polymer anode substrate by the high emission current. Figures 4a and 4b show the  $I$ - $E$  and the corresponding  $F$ - $N$  plots for different bending angles, respectively. The current density of the flat system was  $\sim 0.3$  mA/cm<sup>2</sup>, while it was 0.27 mA/cm<sup>2</sup> for a bending angle of 60° at 1.42 V/ $\mu\text{m}$ .

However, when the sample was allowed to return to its original shape, the emission current density returned to its original value, too. The slopes of the linear F–N regions were also quite similar, regardless of the bending angle. This stable emission is likely owing to the strong adhesion of the 3D rGO emitters to the SWNT-coated PET substrate through strong  $\pi$ – $\pi$  interactions and because of the flexibility of the 3D rGO emitters. An image of the emission from a 3D rGO emitter bent at an angle of 30° is shown in the inset of Fig. 4b; the applied electric field and emission current density were 1.38 V/ $\mu$ m and 0.25 mA/cm<sup>2</sup>, respectively. It can be seen clearly that the electron emission was bright over the entire sample, indicating that the 3D rGO structures were highly crystallized with abundant sharp edges and that there were strong interactions between the rGO emitters and the substrate upon bending.

## Conclusions

We fabricated highly efficient flexible field emitters via the freeze-drying of rGO pastes. The emitters were based on monolithic 3D rGO structures that had protruding tips at the pore edges of the top surface. The pore size and uniformity could be effectively controlled by varying the composition of the rGO/SCMC paste. The density of the protruding graphene edges increased with an increase in the rGO concentration; however, good field-emission characteristics were achieved even at moderately high rGO concentration, owing to the field-screening effect. Al doping decreased the work function of the 3D rGO emitters, which resulted in better field-emission characteristics compared to those of the emitters subjected to Au doping as well as the undoped ones. The stability of the current of the 3D rGO emitters was enhanced by forming a simple coating of ZnO on them. The ZnO layer protected the emission sites of the 3D rGO emitters from the bombardment of the reactive ions of the oxidative gas species. The field emission of the flexible 3D rGO emitters was stable even at high bending angles. This stability was attributed to the high crystallinity and emitter density and good chemical stability of the 3D rGO emitters, as well as to the strong interactions between the 3D rGO emitters and the substrate.

## Experimental

### Preparation of highly concentrated water-based rGO paste

A modified Brodie method was used to synthesize graphite oxide (GO).<sup>52</sup> Pure graphite (2g, Alfa Aesar, 99.999% purity, –200 mesh) was mixed with fuming nitric acid (30 mL) and sodium chlorate (14 g) at room temperature and stirred for 48 h. After the synthesized GO had been washed, a suspension of it was formed in water. The prepared GO (50 mg) was mixed in an aqueous KOH (50 mL) with a pH of 10. The GO was then exfoliated and dispersed using a homogenizer (Unidrive X1000, CAT Scientific) at 12,000 rpm for 2 h.<sup>53</sup> The GO solution was then kept for 6 h under ambient conditions to activate the cation– $\pi$  interactions.<sup>21</sup> Aqueous hydriodic acid (5 mL, HI acid,

Aldrich, 55%, 1 mM) was added to reduce the GO.<sup>54</sup> The mixture was stirred in a homogenizer at 10,000 rpm for 3 h. After being neutralized and centrifuged, the resulting rGO paste-like sediment was decanted.

### Fabrication of a monolithic 3D rGO emitter

rGO pastes of different concentrations were mixed with 1 wt% sodium carboxymethylcellulose (SCMC, Aldrich, molecular weight: 700 K) in a vortex mixer (Wisd VM–10, Daihan Scientific Co.) for 30 min. Small amounts of the rGO pastes were then placed on different substrates, such as indium tin oxide (ITO)-coated glass and single-walled carbon nanotubes (SWNTs)-coated PET, and the substrates were bar coated as shown in Fig. 1b. Subsequently, the paste was freeze dried at –196 °C for 30 min using liquid nitrogen and vacuum dried at  $\sim 10^{-2}$  Torr overnight to sublimate the ice crystals. For chemical doping, an aqueous 1 mM solution of gold chloride (AuCl<sub>3</sub>) and aluminium chloride (AlCl<sub>3</sub>) was mixed with the rGO paste/SCMC mixture. This procedure was performed to synthesize doped 3D rGO emitters. Fabrication of the ZnO protective layer was conducted by a spray coating of ZnO sol on the undoped 3D rGO emitters. The ZnO sol was prepared using diethanolamine as a stabilizer. Anhydrous zinc acetate (6.6 g) and diethanolamine (3.15 g) were stirred in isopropyl alcohol for 30 min. The ZnO sol (20 mL) was deposited on the 3D rGO emitters using an automatic spray coater (NCS-400) with a 1.2 mm nozzle diameter.

### Characterisation

The morphologies of the 3D rGO structures were imaged using field-emission scanning electron microscopy (FESEM, Hitachi S4800) and transmission electron microscopy (TEM, FEI Tecnai G2 F20) at an acceleration voltage of 120 kV. The pore size distribution was measured by image analysis software (Gwyddion version 2.4). The structural characteristics as well as the effects of the doping of the 3D rGO emitters were investigated using confocal Raman spectrometry (NT–MDT, NTEGRA Spectra), which was performed at an excitation wavelength of 532 nm. To confirm the changes in the C1s peaks of the doped 3D rGO emitters, XPS (Multilab2000, Thermo VG Scientific Inc.) was performed using monochromatized Al-K $\alpha$  X-ray radiation. The power was set to 150 W and the voltage to 20 eV to allow for high-resolution scanning; a beam with a diameter of 500  $\mu$ m was used. The work function was measured using UPS, which was performed with a spectrometer equipped with a hemispherical energy analyzer (SES-100, Scienta) and a He I discharge lamp.

### Acknowledgements

H. Y. Kim and S. Jeong contributed equally to this work. This work was supported by the Center for Advanced Soft-Electronics funded by the Ministry of Science, ICT and Future Planning as Global Frontier Project (2014M3A6A5060953), and by the Primary Research Program (14-12-N0101-14 and

14-12-N0101-70) of the Korea Electrotechnology Research Institute. It was also funded in part by the Institute for Basic Science (IBS-R011-D1), South Korea.

## Notes and references

<sup>a</sup>Nano Hybrid Technology Research Center, Korea Electrotechnology Research Institute (KERI), Changwon 642-120, South Korea. E-mail: gwleephd@keri.re.kr

<sup>b</sup>Center for Integrated Nanostructure Physics, Institute for Basic Science, Department of Energy Science, Sungkyunkwan University, Suwon 440-746, South Korea. E-mail: mjeong@skku.edu

<sup>c</sup>Multidimensional Nanomaterials Research Group, Korea Electrotechnology Research Institute (KERI), Changwon 642-120, South Korea. E-mail: wavicle11@keri.re.kr

- G. Eda, H. E. Unalan, N. Rupesinghe, G. A. J. Amaratunga and M. Chhowalla, *Appl. Phys. Lett.*, 2008, **93**, 233502.
- Z.-S. Wu, S. Pei, W. Ren, D. Tang, L. Gao, B. Liu, F. Li, C. Liu and H.-M. Cheng, *Adv. Mater.*, 2009, **21**, 1756.
- H. Yamaguchi, K. Murakami, G. Eda, T. Fujita, P. Guan, W. Wang, C. Gong, J. Boisse, S. Miller, M. Acik, K. Cho, Y. J. Chabal, M. Chen, M. Wakaya and M. Chhowalla, *ACS Nano*, 2011, **5**, 4945.
- A. Wang, J. Wang, P. Miraldo, M. Zhu, R. Outlaw, K. Hou, X. Zhao, B. C. Holloway, D. Manos, T. Tyler, O. Shenderova, M. Ray, J. Dalton and G. McGuire, *Appl. Phys. Lett.*, 2006, **89**, 183103.
- K. Hou, R. A. Outlaw, S. Wang, M. Zhu, R. A. Quinlan, D. M. Manos, M. E. Kordesch, U. Arp and B. C. Holloway, *Appl. Phys. Lett.*, 2008, **92**, 133112.
- L. Jiang, T. Yang, F. Liu, J. Dong, Z. Yao, C. Shen, S. Deng, N. Xu, Y. Liu and H.-J. Gao, *Adv. Mater.*, 2013, **25**, 250.
- S. H. Lee, H. W. Kim, J. O. Hwang, W. J. Lee, J. Kwon, C. W. Bielawski, R. S. Ruoff and S. O. Kim, *Angew. Chem. Int. Ed.*, 2010, **49**, 10084.
- J. M. Yun, K. N. Kim, J. Y. Kim, D. O. Shin, W. J. Lee, S. H. Lee, M. Lieberman and S. O. Kim, *Angew. Chem.*, 2012, **124**, 936.
- H. J. Jeong, H. D. Jeong, H. Y. Kim, S. H. Kim, J. S. Kim, S. Y. Jeong, J. T. Han and G.-W. Lee, *Small*, 2012, **8**, 272.
- H. J. Jeong, H. Y. Kim, H. D. Jeong, S. Y. Jeong, J. T. Han and G.-W. Lee, *J. Mater. Chem.*, 2012, **22**, 11277.
- H. J. Jeong, H. D. Jeong, H. Y. Kim, S. Y. Jeong, J. T. Han and G.-W. Lee, *Small*, 2013, **9**, 2182.
- M. Lazzeri and F. Mauri, *Phys. Rev. Lett.*, 2006, **97**, 266407.
- G. Giovannetti, P. A. Khomyakov, G. Brocks, V. M. Karpan, J. van den Brink and P. J. Kelly, *Phys. Rev. Lett.*, 2008, **101**, 026803.
- J.-H. Chen, C. Jang, S. Adam, M. S. Fuhrer, E. D. Williams and M. Ishigami, *Nat. Phys.*, 2008, **4**, 377.
- Y.-J. Yu, Y. Zhao, S. Ryu, L. E. Brus, K. S. Kim and P. Kim, *Nano Lett.*, 2009, **9**, 3430.
- X. Wang, X. Li, L. Zhang, Y. Yoon, P. K. Weber, H. Wang, J. Guo and H. Dai, *Science*, 2009, **8**, 768.
- D. H. Lee, J. A. Lee, W. J. Lee, D. S. Choi, W. J. Lee and S. O. Kim, *J. Phys. Chem. C*, 2010, **114**, 21184.
- M. L. Yu, B. W. Hussey, H. S. Kim and T. H. Chang, *J. Vac. Sci. Technol. B*, 1994, **12**, 3431.
- H. Zhang, I. Hussain, M. Brust, M. F. Butler, S. P. Rannard and A. I. Cooper, *Nat. Mater.*, 2005, **4**, 787.
- H. Zhang and A. I. Cooper, *Adv. Mater.*, 2007, **19**, 1529.
- S. Y. Jeong, S. H. Kim, J. T. Han, H. J. Jeong, S. Y. Jeong and G.-W. Lee, *Adv. Func. Mater.*, 2012, **22**, 3307..
- L. Qiu, J. Z. Liu, S. L. Y. Chang, Y. Wu and D. Li, *Nat. Commun.*, 2012, **3**, 1241.
- J. H. Chu, J. Kwak, S.-D. Kim, M. J. Lee, J. J. Kim, S.-D. Park, J.-K. Choi, G. H. Ryu, K. Park, S. Y. Kim, J. H. Kim, Z. Lee, Y.-W. Kim and S.-Y. Kwon, *Nat. Commun.*, 2014, **5**, 3383.
- S. Y. Jeong, S. Yang, S. Jeong, I. J. Kim, H. J. Jeong, J. T. Han, K.-J. Baeg and G.-W. Lee, *Small*, 2015, DOI: 10.1002/sml.201403085.
- N. D. Luong, N. Pahimanolis, U. Hippi, J. T. Korhonen, J. Ruokolainen, L. Johansson, J. Nam and J. Seppala, *J. Mater. Chem.*, 2011, **21**, 13991.
- W. Kulicic, U. Reinhardt, G. G. Fuller and O. Arendt, *Rheol. Acta*, 1999, **38**, 26.
- S. Deville, E. Saiz and A. O. Tomsia, *Acta Mater.*, 2007, **55**, 1965.
- M. F. Butler, *Cryst. Growth Des.*, 2002, **2**, 59.
- M. C. Gutiérrez, Z. Y. García-Carvajal, M. Jobbágy, F. Rubio, L. Yuste, F. Rojo, M. L. Ferrer and F. del Monte, *Adv. Funct. Mater.*, 2007, **17**, 3505.
- M. Qian, T. Feng, H. Ding, L. Lin, H. Li, Y. Chen and Z. Sun, *Nanotechnology*, 2009, **20**, 425702; J. Wang, M. Zhu, X. Zhao, R. A. Outlaw, D. M. Manos, B. C. Holloway, C. Park, T. Anderson and V. P. Mammanna, *J. Vac. Sci. Technol. B*, 2004, **22**, 1269.
- V. P. Verma, S. Das, I. Lahiri, W. Choi, *Appl. Phys. Lett.*, 2010, **96**, 203108; I. Lahiri, V. P. verma, W. Choi, *Carbon*, 2011, **49**, 1614; Z. Yan, L. Ma, Y. Zhu, I. Lahiri, M. G. Hahm, Z. Liu, S. Yang, C. Xiang, W. Lu, Z. Peng, Z. Sun, C. Kittrell, J. Lou, W. Choi, J. M. Tour, *ACS Nano*, 2013, **7**, 58.
- L. Nilsson, O. Groening, C. Emmenegger, O. Kuettel, E. Schaller, L. Schlapbach, H. Kind, J.-M. Bonard and K. Kern, *Appl. Phys. Lett.*, 2000, **76**, 2071.
- J. S. Suh, K. S. Jeong, J. S. Lee and I. Han, *Appl. Phys. Lett.*, 2002, **80**, 2392.
- D. H. Lee, J. A. Lee, W. J. Lee and S. O. Kim, *Small*, 2011, **7**, 95.
- R. H. Fowler and L. Nordheim, *Proc. R. Soc. London, Ser. A*, 1928, **119**, 173.
- A. Das, S. Pisana, B. Chakraborty, S. Piscanec, S. K. Saha, U. V. Waghmare, K. S. Novoselov, H. R. Krishnamurthy, A. K. Geim, A. C. Ferrari and A. K. Sood, *Nat. Nanotechnol.*, 2008, **3**, 210.
- A. C. Ferrari, *Solid State Commun.*, 2007, **143**, 47.
- U. Dettlaff-Weglikowska, V. Skákalová, R. Graupner, S. H. Jhang, B. H. Kim, H. J. Lee, L. Ley, Y. W. Park, S. Berber, D. Tománek and S. Roth, *J. Am. Chem. Soc.*, 2005, **127**, 5125.
- H.-J. Shin, S. M. Kim, S.-M. Yoon, A. Benayad, K. K. Kim, S. J. Kim, H. K. Park, J.-Y. Choi and Y. H. Lee, *J. Am. Chem. Soc.*, 2008, **130**, 2062.
- H.-Z. Geng, K. K. Kim, C. Song, N. T. Xuyen, S. M. Kim, K. A. Park, D. S. Lee, K. H. An, Y. S. Lee, Y. Chang, Y. J. Lee, J. Y. Choi, A. Benayad and Y. H. Lee, *J. Mater. Chem.*, 2008, **18**, 1261.
- G. Giovannetti, P. A. Khomyakov, G. Brocks, V. M. Karpan, J. van den Brink and P. J. Kelly, *Phys. Rev. Lett.*, 2008, **101**, 026803.

- 42 J. O. Hwang, D. H. Lee, J. Y. Kim, T. H. Han, B. H. Kim, M. Park, K. No and S. O. Kim, *J. Mater. Chem.*, 2011, **21**, 3432.
- 43 Y. Shi, K. K. Kim, A. Reina, M. Hofmann, L.-J. Li and J. Kong, *ACS Nano*, 2010, **4**, 2689.
- 44 F. Günes, H.-J. Shin, C. Biswas, G. H. Han, E. S. Kim, S. J. Chae, J.-Y. Choi and Y. H. Lee, *ACS Nano*, 2010, **4**, 4595.
- 45 I. Gierz, C. Riedl, U. Starke, C. R. Ast and C. Kern, *Nano Lett.*, 2008, **8**, 4603.
- 46 J. M. Bonard, J. P. Salvetat, T. Stockli, W. A. de Heer, L. Forro and A. Chatelain, *Appl. Phys. Lett.*, 1998, **73**, 918.
- 47 S. C. Lim, Y. C. Choi, H. J. Jeong, Y. M. Shin, K. H. An, D. J. Bae, Y. H. Lee, N. S. Lee and J. M. Kim, *Adv. Mater.*, 2001, **13**, 1563.
- 48 J. T. Han, B. G. Kim, M. Yang, J. S. Kim, H. J. Jeong, S. Y. Jeong, S.-H. Hong and G.-W. Lee, *ACS Appl. Mater. Interfaces*, 2011, **3**, 2671.
- 49 W. H. Hirschwald, *J. Am. Chem. Soc.*, 1985, **18**, 228.
- 50 Y.-S. Min, E. J. Bae, U. J. Kim, W. Park and C. S. Hwang, *Appl. Phys. Lett.*, 2006, **89**, 113116.
- 51 H. J. Jeong, H. D. Jeong, H. Y. Kim, J. S. Kim, S. Y. Jeong, J. T. Han, D. S. Bang and G.-W. Lee, *Adv. Funct. Mater.*, 2011, **21**, 1526.
- 52 B. C. Bridie, *Philos. Trans. R. Soc. London*, 1859, **149**, 249.
- 53 S. Y. Jeong, S. H. Kim, J. T. Han, H. J. Jeong, S. Yang and G.-W. Lee, *ACS Nano*, 2011, **5**, 870.
- 54 I. K. Moon, J. Lee, R. S. Ruoff and H. Lee, *Nat. Commun.*, 2010, **1**, 73.